# Estimating accuracy in optimal deconvolution of synthetic AMSR-E observations

Ashutosh S. Limaye *, William L. Crosson, Charles A. Laymon

*Universities Space Research Association, NSSTC, 320 Sparkman Dr., Huntsville, AL 35805, United States*

## Abstract

Optimal deconvolution (ODC) utilizes the footprint overlap in microwave observations to estimate the earth's brightness temperatures ($T_B$). This paper examines the accuracy of ODC-estimated $T_B$ compared with a standard averaging technique. Because brightness temperatures cannot be independently verified, we constructed synthetic True $T_B$ for accuracy assessment. We assigned $T_B$ at a high spatial resolution (1 km) grid and computed the True $T_B$ by spatial averaging of the assigned $T_B$ to a lower resolution earth grid (25 km), selected to match the resolution of products generated from the Advanced Microwave Scanning Radiometer for the Earth Observing System (AMSR-E). We used the sensor antenna response function along with the 1-km assigned $T_B$ to generate synthetic observations at AMSR-E footprint locations. These synthetic observations were subsequently deconvolved in the ODC technique to estimate $T_B$ at the lower resolution earth grid. The ODC-estimated $T_B$ and the simple grid cell averages of the synthetic observations were compared with the True $T_B$ allowing us to quantify the efficacy of each technique. In areas of high $T_B$ contrast (such as boundaries of water bodies), ODC performed significantly better than averaging. In other areas, ODC and averaging techniques produced similar results. A technique similar to ODC can be effective in delineating water bodies with significant clarity. That will allow microwave observations to be utilized near the shorelines, a trouble spot for the currently used averaging techniques.
© 2005 Elsevier Inc. All rights reserved.

*Keywords:* Optimal; Deconvolution; Microwave; Radiometer; AMSR-E; Synthetic

## 1. Introduction

Satellite microwave radiometer observations may be expressed as convolutions of the sensor antenna response function with the earth's brightness temperature ($T_B$) field, integrated over the sensor footprint. However, in many applications, these observations are treated as point measurements and are averaged (Njoku, 2004; Njoku et al., 2003) to produce gridded spatial representations of the observed $T_B$ at coarser resolution than the spacing of the observations. Because adjacent observations have significant footprint overlap, averaging the observations in this way leads to smoothing of surface boundaries and obscures small surface features. Stogryn (1978) utilized the overlap to estimate

observational data at locations within the overlap, using a deconvolution approach to match the antenna response functions of adjacent observations. Poe (1990) presented an optimal interpolation method based on the Stogryn technique. The focus of that research was to optimally interpolate the observations using the information in the overlap without any spatial resolution enhancement. Farrar and Smith (1992) matched observations made at different frequencies in a multi-frequency analysis to obtain higher resolution observations. Robinson et al. (1992) and Mo (1999) presented similar techniques to increase the spatial resolution as well as to apply antenna pattern corrections. All of these investigations focused on antenna pattern matching to optimally generate observations at other earth surface locations, not on an earth grid. By contrast, the focus of this study is deconvolution of microwave observations to produce more accurate brightness temperatures on an earth grid. We hypothesize that the accuracy of estimation of radiometer $T_B$ at a specified grid resolution can

---

* Corresponding author. Tel.: +1 256 961 7903.
  *E-mail address:* Ashutosh.Limaye@msfc.nasa.gov (A.S. Limaye).

be improved by application of an optimal deconvolution (ODC) technique.

Limaye et al. (2004) explored an ODC technique for airborne radiometer data collected during Soil Moisture Experiment 2002 (SMEX02, Cosh et al., 2004). In that study, the authors used data from Passive and Active L and S band radiometer (PALS; Wilson et al., 2001), and showed that the ODC technique results in significant improvements over the conventional techniques with mean absolute and root mean square error reductions of approximately 60% and 50%, respectively. During SMEX02, PALS was used to scan along track only and the authors did not need to account for the azimuthal variations in the data. The work presented in this study generalizes the approach taken earlier

by the authors (Limaye et al., 2004) to account for the complexities presented by the azimuth variations in the data collected by conically scanning radiometers. Accurate estimation of $T_B$ is critical for many applications including retrievals of soil moisture, sea ice extent, and snow cover (Cavalieri et al., 1997; Crosson et al., 2005; Laymon et al., 2001).

In order to evaluate the accuracy of ODC-estimated $T_B$ with respect to a benchmark method (Averaging), it is necessary to compare brightness temperatures estimated using both methods to the 'true' or known $T_B$ at this scale. Use of actual AMSR-E $T_B$ observations will not permit this type of evaluation because the $T_B$ observations represent the convolution of the surface $T_B$ field and the antenna gain function, therefore the 'true' mean
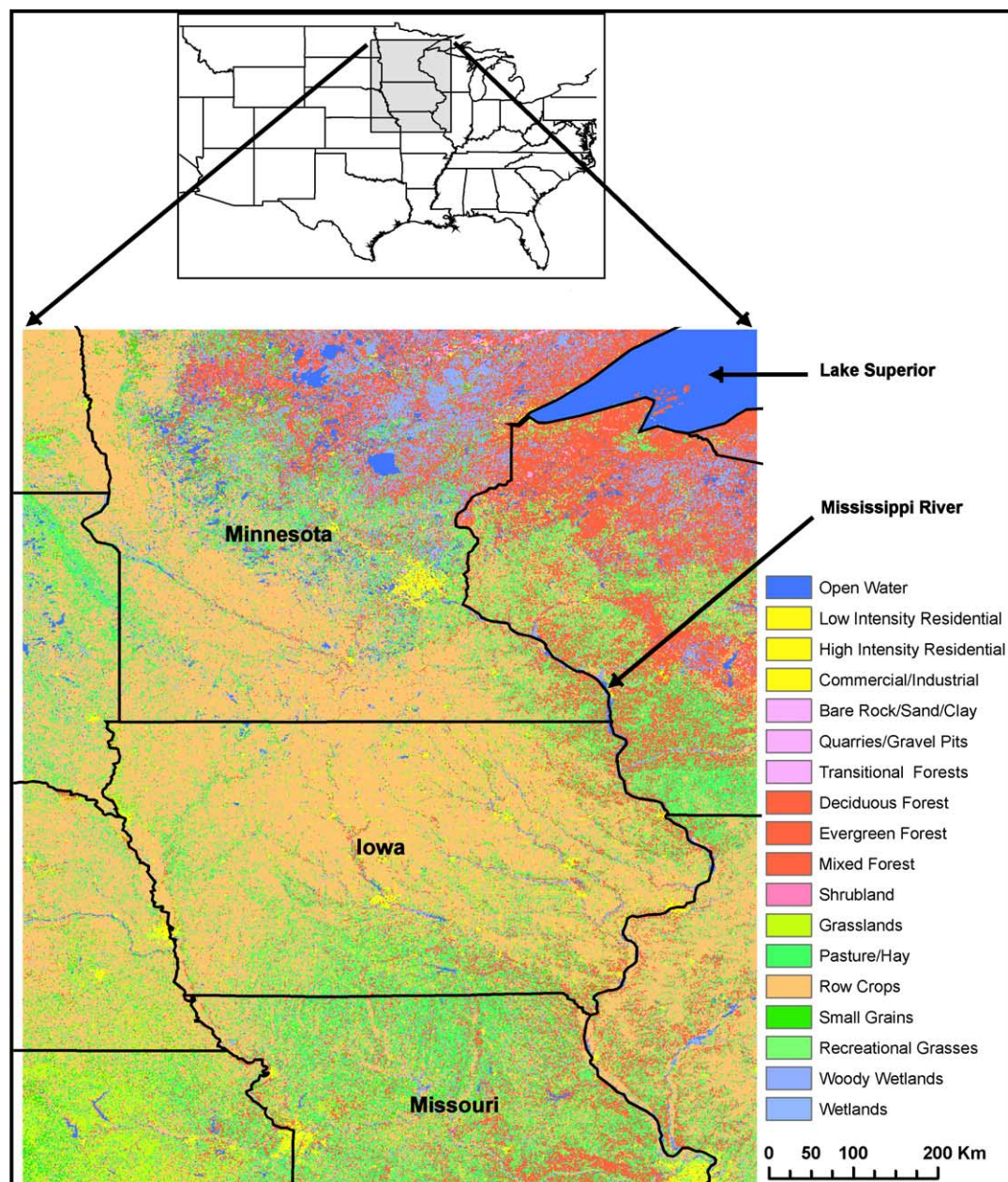


Fig. 1. Location and land cover classification of the study area.

$T_B$ for a specified region on the Earth's surface is not recoverable from the measurements. We have chosen to generate synthetic $T_B$ fields over a large central U.S. domain in order to perform this evaluation. Using this approach also allows testing of the ODC technique under various assumptions regarding the spatial nature of $T_B$.

## 2. Study area

The domain covers the eastern portions of the Great Plains states eastward to the Midwestern U.S., including the western extent of Lake Superior (Fig. 1). The land cover at 1-km spatial resolution (National Land Cover Dataset (NLCD), Vogelmann et al., 1998) is also shown. The dominant land cover classes in the southwestern corner of the domain are grasslands and pasture/hay. The central portion of the region primarily comprises of row crops. In the northeastern area there is a mix of forests, open water and wetlands. Approximately 4.2% of the entire study area is open water, almost all of which is concentrated in the northeastern region. Areas in yellow indicate urbanized land uses.

## 3. Optimal deconvolution

### 3.1. Oversampling of microwave observations

The basic premise of the ODC technique (Limaye et al., 2004) was to utilize the overlap in adjacent microwave radiometer observation footprints. Adjacent observations cover mostly the same target features on the ground (e.g., grid cells), but with different contributions to the overall signal. That overlap can be effectively utilized to more accurately estimate the $T_B$ of those grid cells. Typically, the observations far outnumber the grid cells (for which we want to estimate the unknown $T_B$). Because there are more equations than unknowns, the system of equations does not have a unique solution. The optimal deconvolution technique is one way to arrive at the optimal solution.

Knowing the sensor characteristics (altitude, incidence angle, half power beam width and the shape of the sensor antenna response function), we can map the region from which the energy was received. The spatial characteristics of the function vary for each sensor. We have assumed a Gaussian response function for the purpose of this study, given by:

$$P(r) = \frac{1}{\sigma\sqrt{2\pi}} e^{\frac{-r^2}{2\sigma^2}}. \tag{1}$$

The shape of the function is defined by $\sigma^2$ and can be computed knowing the half power beam width. The power $P$ in Eq. (1) is at the radial distance $r$ on the beam-normal plane. In most microwave radiometer applications, the sensors are positioned at non-nadir angles, and therefore the beam-normal plane is not coincident with the earth surface. It is therefore necessary to project the grid points from the earth's surface onto the beam-normal plane.

### 3.2. Projections to the beam-normal plane

If the origin of our 3-D space is the location where the beam intersects the ground, the sensor location can be given by $(X_s, Y_s, H)$, where $H$ is the altitude of the sensor. If the sensor incidence angle is $\theta$ and the sensor azimuth angle is $\phi$, then

$$X_s = H\tan(\theta)\cos(\phi) \tag{2}$$

$$Y_s = H\tan(\theta)\sin(\phi) \tag{3}$$

The equation of the plane going through the origin and normal to the beam is given by

$$X_s X + Y_s Y + HZ = 0. \tag{4}$$

Substituting the sensor location into the equation above gives

$$\tan(\theta)\cos(\phi)X + \tan(\theta)\sin(\phi)Y + Z = 0. \tag{5}$$

Any point $(X_1, Y_1, 0)$ on the earth surface can be projected onto the beam-normal plane by solving Eq. (5) and the parametric representation of the vector from the sensor location $(X_s, Y_s, H)$ to the point on the horizontal surface $(X_1, Y_1, 0)$. The projected point on the beam-normal plane is given by

$$X_p = \frac{(X_1 Y_s - X_s Y_1)\sin\phi + X_1 H\cot\theta}{(X_s - X_1)\cos\phi + (Y_s - Y_1)\sin\phi + H\cot\theta} \tag{6}$$

$$Y_p = \frac{(X_s Y_1 - X_1 Y_s)\cos\phi + Y_1 H\cot\theta}{(X_s - X_1)\cos\phi + (Y_s - Y_1)\sin\phi + H\cot\theta} \tag{7}$$

$$Z_p = -\frac{HX_1\cos\phi + Y_1 H\sin\phi}{(X_s - X_1)\cos\phi + (Y_s - Y_1)\sin\phi + H\cot\theta} \tag{8}$$

The distance from the point $(X_p, Y_p, Z_p)$ on the beam-normal plane to the origin is then given by:

$$r = \sqrt{X_p^2 + Y_p^2 + Z_p^2}. \tag{9}$$

### 3.3. Creation of AMSR-E synthetic $T_B$ observations

Eqs. (1) and (9) define the sensor antenna response function on the horizontal surface. As described later in Section 4, we generated four different synthetic surface brightness temperature fields over the study region. In order to simulate remote sensing observations based on these $T_B$ fields, we use this sensor antenna response function (hereafter called the weighting function) to numerically integrate energy received at the sensor. This step is referred to as convolution. These synthetic $T_B$ observations are intended to simulate level 2A observations from NASA's Advanced Microwave Scanning Radiometer for the Earth Observing System (AMSR-E). In processing of the AMSR-E data, level 2A observations are averaged by the AMSR-E operational algorithm. For averaging, the algorithm uses a grid called the EASE grid defined by National Snow and Ice Data Center (NSIDC, 2002). Averaging of level 2A observations centered over each 25 km

EASE grid cell produces level 2B $T_B$ for that cell, and is subsequently used to produce the remotely sensed soil moisture estimate at that EASE grid cell (Njoku, 2004). In this study, we use the same EASE grid for the analysis. For the generation of synthetic $T_B$ observations, we used a 1 km land use dataset nested within each 25 km EASE grid cell. We use the actual observation locations from an AMSR-E overpass and the associated sensor orientation geometry for this analysis. The $T_B$ data associated with the observation location was derived from the assignments at the 1-km grid (described in detail in Section 4).

In real world application of the ODC technique, actual observations would replace the synthetic observations. The only information needed for the use of ODC technique with the actual level 2A AMSR-E observations would be the sensor geometry (incidence angle, earth azimuth angle, altitude, geolocation of the beam intersection on the ground).

## 3.4. Optimal solution

In order to deconvolve synthetic $T_B$ observations to produce gridded brightness temperatures on the earth's surface, we overlaid the weighting function onto the EASE grid cells. A critical element in this analysis is the estimation of the fractional contribution of each EASE grid cell to the overall observation. It is computed by integrating the volume under the Gaussian response function for each EASE grid cell within the spatial extent of the weighting function. Adjacent observations convolve from similar EASE grid cells, but have different fractional contributions from each of the EASE grid cells. Typically, 25 to 29 EASE grid cells contribute to an

Table 1
Baseline brightness temperature values specified for each USGS National Land Cover Dataset (NLCD) land cover class

| Landcover class | $T_B$ (K) |
| --- | --- |
| Open water | 175 |
| Low intensity residential | 270 |
| High intensity residential | 250 |
| Commercial/industrial/transportation | 250 |
| Bare rock/sand/clay | 250 |
| Quarries/strip mines/gravel pits | 250 |
| Transitional | 250 |
| Deciduous forest | 290 |
| Evergreen forest | 290 |
| Mixed forest | 290 |
| Shrubland | 270 |
| Orchards/vineyards/other | 270 |
| Grasslands/herbaceous | 270 |
| Pasture/hay | 270 |
| Row crops | 275 |
| Small grains | 260 |
| Fallow | 250 |
| Urban/recreational grasses | 270 |
| Woody wetlands | 270 |
| Emergent herbaceous wetlands | 270 |

observation in varying fractions. Given the large extent of the sensor footprint (as can be seen in Fig. 2), the maximum fractional contribution from an EASE grid cell to an observation is approximately 0.14. In other words, the EASE grid cell containing the observation contributed only 14% of the total energy received for that observation. The Gaussian surface extends to infinity, and for the sake of this analysis, we ignore fractional contributions smaller than 0.001. Because the sum of all the fractional contributions needs to be 1, the
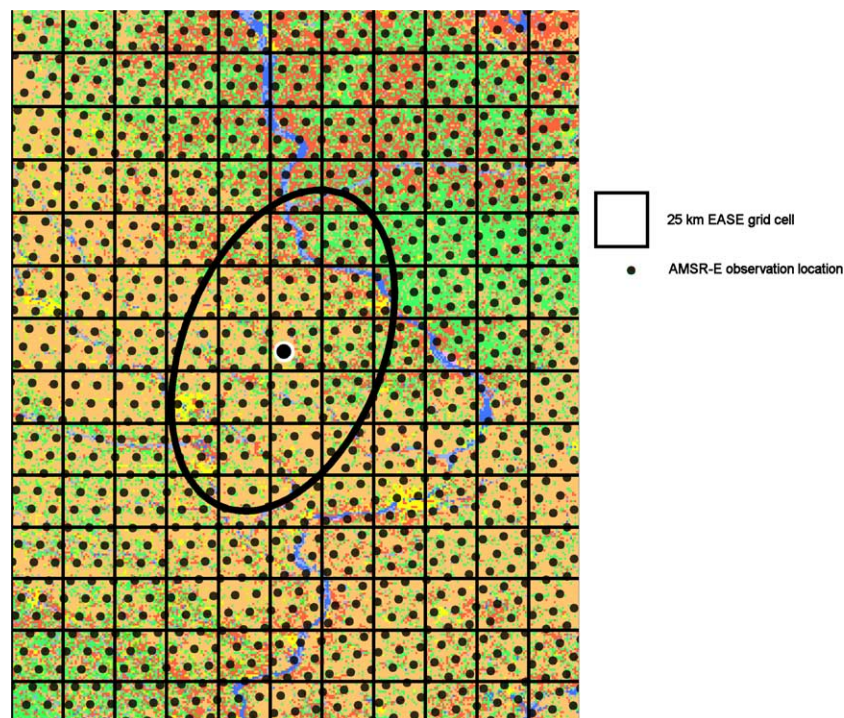


Fig. 2. Graphical representation of AMSR-E sensor antenna response function's spatial extent (shown as the oval with the black dot in the center depicting the beam center location) in relation to the EASE grid cells and other AMSR-E observation locations.
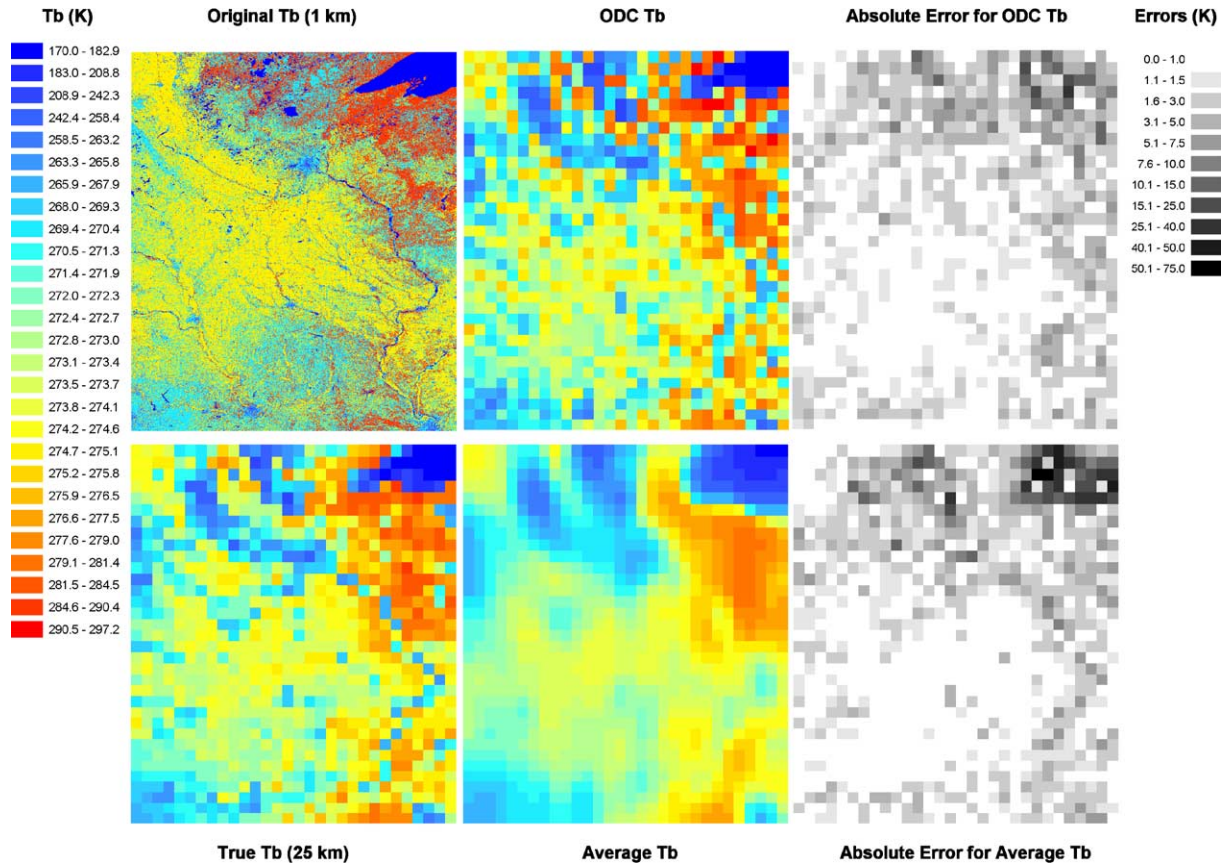
Fig. 3. Baseline scenario comparing True $T_B$ with ODC estimated and Average $T_B$.

ignored fractional contributions are proportionately distributed among the remaining cells.

Optimization is intended to solve for the $T_B$ for the EASE grid cells, the unknown variables in this analysis. The known quantities are the observations (synthetic in the case of this study, actual observations in real world scenarios) and the fractional contributions from the EASE grid cells in that observation's field of view. The product of the fractional contribution from each EASE grid cell with the unknown $T_B$ for that cell is the $T_B$ input of that EASE grid cell to the overall reconstructed observation. Integration of all such $T_B$ inputs from individual EASE grid cells in the weighting function results in estimation of the reconstructed observation. Because the intended purpose of the reconstructed observation is to reproduce the synthetic observation, we need to minimize the difference between the two. The optimization problem is given by:

$$\text{Minimize} \sum_n \text{abs}(\text{Reconstructed} - \text{Synthetic } T_B) \qquad (10)$$

where $n$ is the number of observations. The equation for the reconstructed observation serves as the constraint for the minimization, given by:

$$\text{Reconstructed Observation} = \sum_{\text{all EASEgrid cells in field of view}}$$

$$\times (\text{Fractional Contribution})_m * (T_B)_m \qquad (11)$$

where $m$ represents the EASE grid cells in the observation's field of view. For the study area, which included about 1000 EASE grid cells, AMSR-E typically records about 6500 observations. In other words, there are 6500 reconstructed observation equations for the 1000 unknown EASE grid cell $T_B$ values. Thus, we have more equations than unknowns, forcing us to use an optimization to solve for the unknown variables. The minimization criterion forces the reconstructed observations to be as close to the synthetic observations as possible. Eqs. (10) and (11) form a system of linear equations, an iterative solution of which results in the estimation of the $T_B$ for the EASE grid cells (referred to here as ODC-estimated $T_B$).

Eqs. (6), (7), and (8) require the knowledge of sensor azimuth angle ($\phi$) for each observation. It allows for accounting for the azimuthal variability in the brightness temperatures from grid cells. In real world analysis, it may be desired to analyze the $T_B$ for specific azimuth angles in order to isolate anisotropy in observations. While the analysis presented here does not discriminate among $T_B$ from different azimuth angles, it can be performed for selected azimuth angles if desired.

## 4. Synthetic scenarios

We have generated four synthetic $T_B$ fields over the study domain and used them to quantify the errors associated with

the ODC and averaging techniques. In each case, $T_B$ values were specified at the 1 km NLCD land cover grid scale nested within the 25 km EASE grid. This 1 km grid $T_B$ is hereafter called the Original $T_B$.

### 4.1. Baseline

Brightness temperatures in the Baseline scenario are determined by assignment based on NLCD land cover class. The default brightness temperatures for all the classes are shown in Table 1. These values were set to represent in a general sense the typical C and X band $T_B$ differences that arise from vegetation density differences between land cover classes. The assigned $T_B$ range from 175 K for water to 290 K for forest. In the three additional scenarios described below, $T_B$ anomalies were superimposed on the Baseline $T_B$ values based on specific patterns.

### 4.2. Gradient

In this scenario, a maximum $T_B$ anomaly of $+25$ K was imposed at the northwest corner of the domain, and values decreased linearly toward the southeast corner. The anomaly in the southeast corner was $-25$ K. Anomalies were added to the default $T_B$ values at each 1 km sub-grid cell. The northwest–southeast gradient was designed to distinguish the effects of the $T_B$ gradient from the grid orientation.

### 4.3. Minimum

This case simulates a situation in which $T_B$ is at a minimum at the center of the study area and increases with distance from the center to maxima in the corners. At the center, a $T_B$ anomaly of $-15$ K was imposed on the default $T_B$ values for each land cover class at the 1 km scale. A $T_B$ gradient in both ordinal directions was applied so that anomalies of $+15$ K were realized on the edges of the domain directly east, west, north or south of the center. Slightly higher anomalies were simulated in the corners of the domain due to the greater distances from the central point. This scenario could be considered analogous to a mesoscale rain event in the middle of the study area.

### 4.4. Random

In this scenario, normal random deviates with a mean of 0 and a standard deviation of 10 K were generated and the scenario was made more extreme by assigning one random deviate for each EASE grid cell. Within an EASE grid cell, all 1 km cells were adjusted from the default $T_B$ using the random deviate. No spatial autocorrelation in the random component of $T_B$ was assumed between EASE grid cells.

We superimposed each $T_B$ scenario with an actual AMSR-E overpass, i.e. the level 2A observation locations where the beam intersects the ground for a typical day were used in a comparison of the ODC and Averaging methods. For the
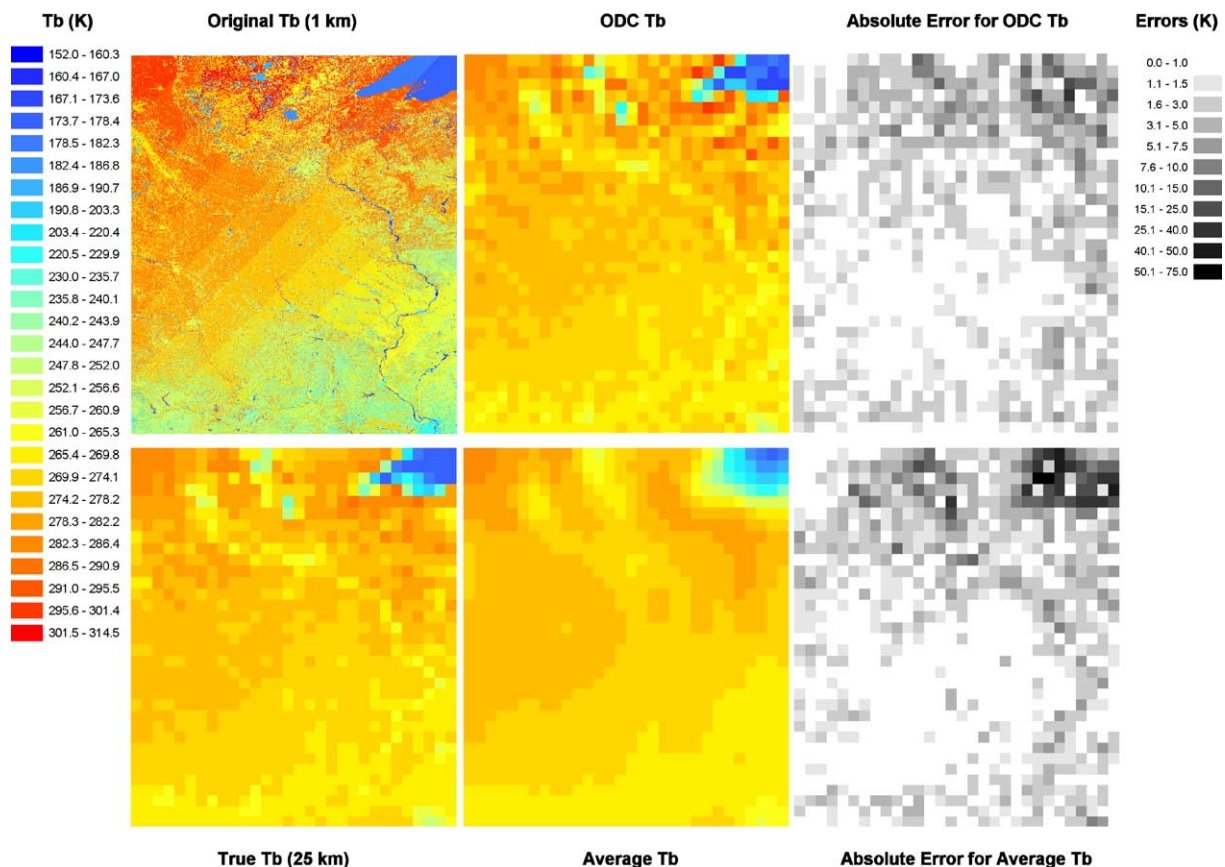


Fig. 4. Gradient scenario comparing True $T_B$ with ODC estimated and Average $T_B$.

analysis presented here, observation locations from the ascending pass on June 25, 2002 were used. Fig. 2 shows the elliptical area from which over 90% of the energy is received at the sensor. The other black points are adjacent AMSR-E beam center locations, the density of which illustrates the significant overlap of the adjacent observations. The grid shown is the AMSR-E EASE grid with a spatial resolution of 25 km, and the underlying NLCD data is on a 1 km high-resolution grid nested within the EASE grid. Assuming a Gaussian response function, we integrated the product of the Original $T_B$ with the power (computed using Eq. (1)) to 'reconstruct' the sensor observation. Using Eqs. (10) and (11), we develop a system of equations to generate the reconstructed observations. Simultaneous solution of this system of equations generates the solution for the unknown EASE grid cell $T_B$ (ODC estimated $T_B$).

## 5. Results

We have evaluated the accuracy of ODC-derived $T_B$ in comparison to the accuracy of one currently used methodology, Averaging. In the current process, all the AMSR-E level 2A observations within an EASE grid cell are averaged to produce the level 2B product (Njoku, 2004). The level 2B product is subsequently used in the soil moisture retrieval algorithm. Similarly for this analysis, we computed the averages of all the synthetic observations located within an EASE grid cell and refer to this quantity as the Average $T_B$. We compared ODC and Average $T_B$ with the True $T_B$, computed as the average of the 625 1-km Original $T_B$ values within each EASE grid cell, allowing us to assess the relative accuracies of the two gridding methods.

Figs. 3–6 provide the spatial representation of the four scenarios considered in this analysis. Each figure consists of six panels. The upper left panel is the Original $T_B$ at 1 km resolution. The convolution at each AMSR-E observation location is performed using the Original $T_B$ field to produce synthetic observations. True $T_B$ (lower left panel), computed by averaging the Original $T_B$ within each 25 km EASE grid cell, is used to assess the accuracy of ODC-estimated $T_B$ as well as Average $T_B$. ODC estimated $T_B$ is shown in the upper middle panel and Average $T_B$ is shown in lower middle panel. The upper right panel shows the absolute error between True and ODC-estimated $T_B$ whereas the lower right panel shows the absolute error between True and Average $T_B$.

In the absence of a land cover bias, an estimation technique should exactly reproduce the True $T_B$. If land cover bias is removed (with completely random $T_B$ assignments in an EASE grid cell), the ODC technique does indeed reproduce the True $T_B$ (not shown here). However in reality, each EASE grid cell is made up of discrete (and thus non-random) land cover components with significant $T_B$ differences among the components. Therefore the same EASE grid cell can have substantially different $T_B$ contributions to observations looking at different parts of the same EASE grid cell. The reconciliation
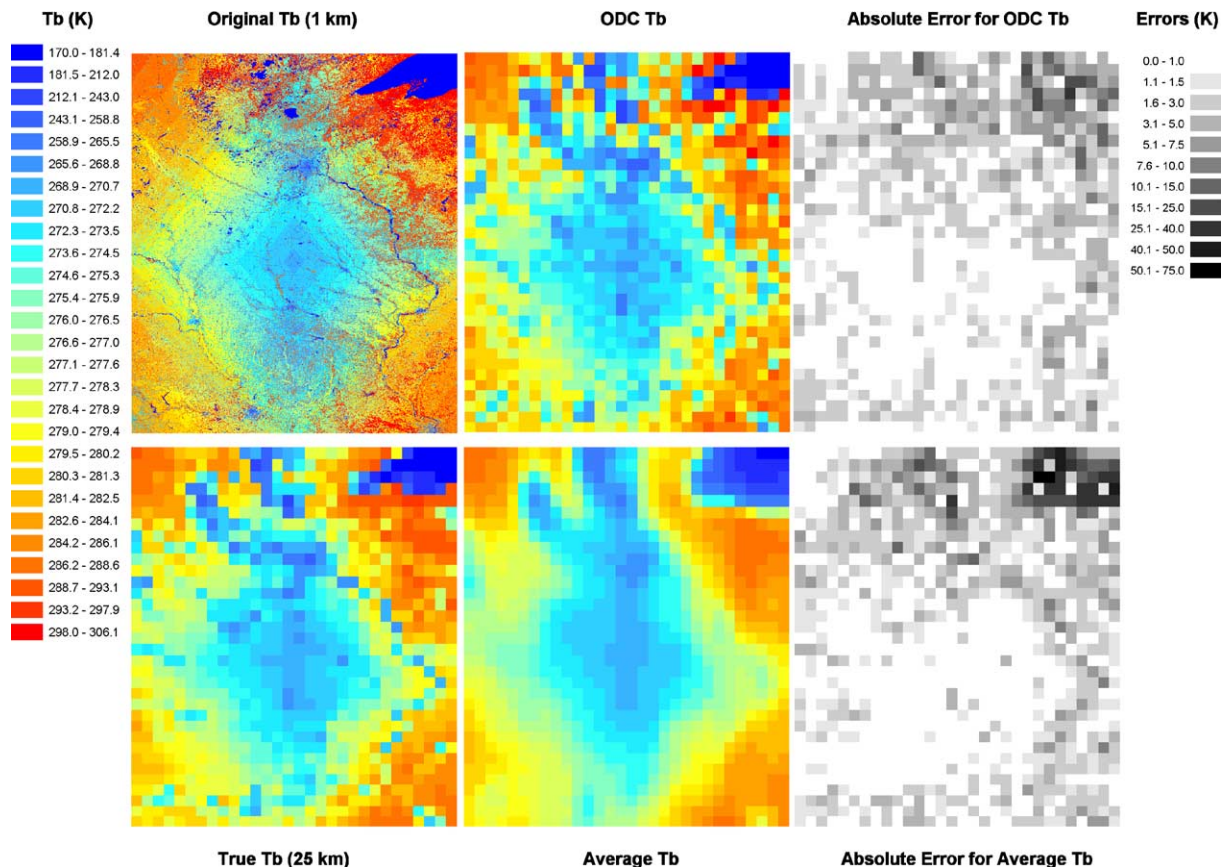


Fig. 5. Minimum scenario comparing True $T_B$ with ODC estimated and Average $T_B$.
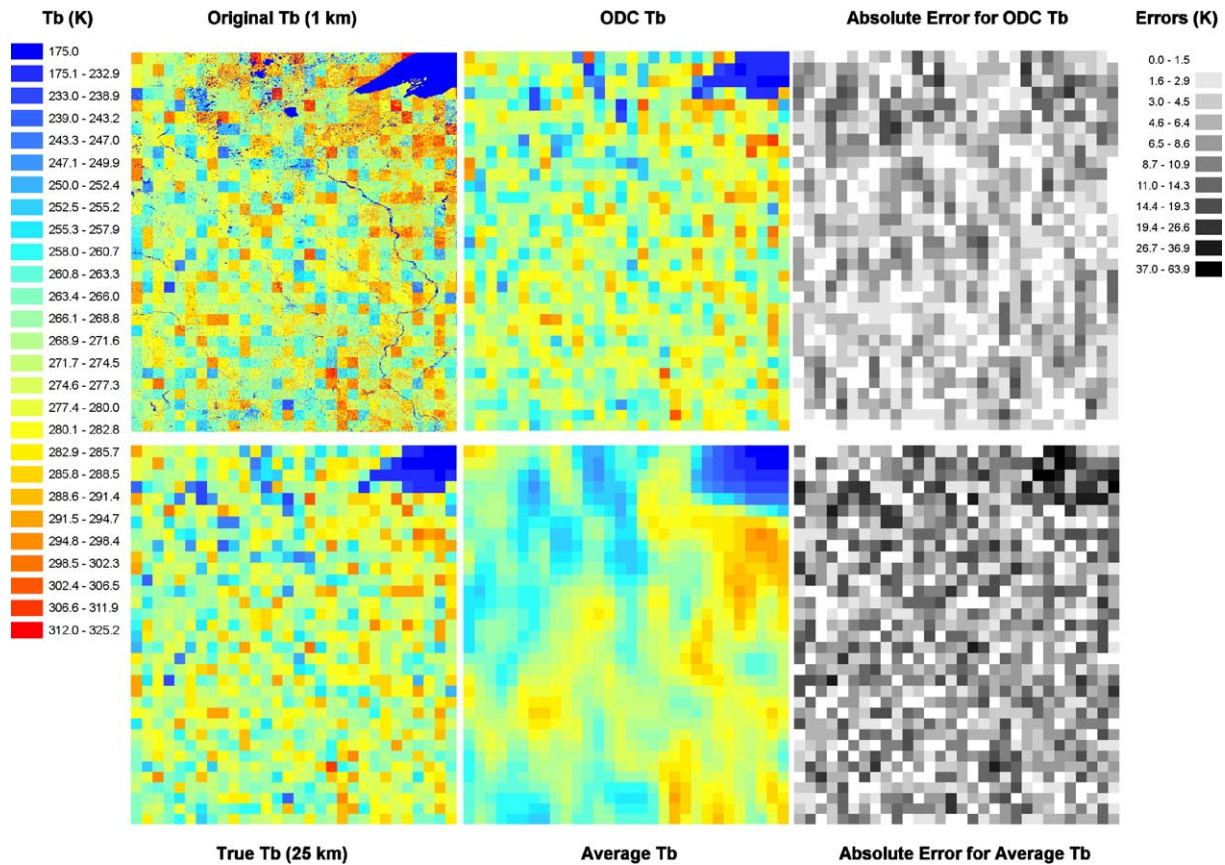
Fig. 6. Random scenario comparing True $T_B$ with ODC estimated and Average $T_B$.

of these different $T_B$ contributions becomes an optimality challenge.

Fig. 3 shows the Baseline scenario, in which default $T_B$ assignments were made for each 1 km cell based on the NLCD classes. It can be seen that the ODC $T_B$ reproduces the fine-scale spatial representation of True $T_B$ better than the Average, which presents a smooth field. ODC technique defined Lake Superior in the northeast corner of the study area better than the Average technique, which produces a diffused and larger region of lower $T_B$. The Mississippi River can be traced in the Original as well as True $T_B$ panels, and can also be discerned in the ODC estimated $T_B$, whereas it is not visible in the Average $T_B$ image. As shown in Table 2, the ODC technique produces significantly lower mean absolute errors (MAE) than that for the Average in the northern half of the region, which is dominated by lakes (2.49 K for ODC technique as compared to 3.92 K for the Averaging technique). MAE is very slightly higher in ODC (1.08 K) than in Average (1.05 K) in the southern half of the study area, but that difference is not

statistically significant. ODC technique performs substantially better than Averaging technique in root mean square error (RMSE) as shown in Table 3.

Fig. 4 shows the Gradient scenario in which a northwest–southeast $T_B$ gradient is imposed. As in the case of Baseline scenario, the water body and the river are better defined in the ODC $T_B$ than in the Average $T_B$. The mean absolute errors for ODC are also lower than for Average $T_B$ in the northern half and slightly higher in the southern half. Fig. 5 shows a Minimum scenario, and the results are similar to the other two scenarios. The ODC technique reproduced the details of the $T_B$ minimum in the middle of the study area better than the Average technique while still maintaining the ability to define the river. Fig. 6 shows the Random scenario, in which a random $T_B$ anomaly was added to the base $T_B$ for each cell. ODC performs much better than the Averaging method in this scenario over both halves of the study region.

Table 4 shows that the ODC statistics are better than the Averaging technique for each of the four scenarios. The means

Table 2
Mean Absolute errors for each scenario for the entire domain and the northern and southern halves

|  | Base | | Gradient | | Minimum | | Random | |
|---|---|---|---|---|---|---|---|---|
|  | ODC | Avg | ODC | Avg | ODC | Avg | ODC | Avg |
| All (K) | 1.78 | 2.49 | 1.81 | 2.52 | 1.92 | 2.65 | 4.61 | 7.72 |
| Northern half (K) | 2.49 | 3.92 | 2.56 | 4.01 | 2.73 | 4.19 | 5.11 | 8.65 |
| Southern half (K) | 1.08 | 1.05 | 1.06 | 1.03 | 1.10 | 1.12 | 4.12 | 6.80 |

Table 3
Root mean square errors for each scenario for the entire domain and the northern and southern halves

|  | Base | | Gradient | | Minimum | | Random | |
|---|---|---|---|---|---|---|---|---|
|  | ODC | Avg | ODC | Avg | ODC | Avg | ODC | Avg |
| All (K) | 2.99 | 5.94 | 2.99 | 6.04 | 3.26 | 6.44 | 6.00 | 10.37 |
| Northern half (K) | 3.95 | 8.25 | 3.96 | 8.40 | 4.32 | 8.96 | 6.64 | 11.90 |
| Southern half (K) | 1.53 | 1.58 | 1.50 | 1.54 | 1.59 | 1.67 | 5.29 | 8.56 |

Table 4
Means, ranges and standard deviations for True, ODC-estimated and Average $T_B$ over the study area, and $r^2$ values for ODC-estimated and Average $T_B$ with respect to the True $T_B$

|  | Base | | | Gradient | | | Minimum | | | Random | | |
|---|---|---|---|---|---|---|---|---|---|---|---|---|
|  | True | ODC | Avg | True | ODC | Avg | True | ODC | Avg | True | ODC | Avg |
| Mean (K) | 270.9 | 270.9 | 270.9 | 271.7 | 271.2 | 271.1 | 275.3 | 275.3 | 275.3 | 270.8 | 270.8 | 270.8 |
| Range (K) | 111.2 | 127.2 | 102.5 | 112.5 | 127.5 | 105.7 | 121.3 | 136.1 | 109.9 | 131.6 | 140.2 | 105.9 |
| SD (K) | 13.5 | 14.2 | 10.8 | 13.8 | 14.5 | 11.1 | 14.5 | 15.2 | 11.5 | 16.5 | 16.5 | 11.2 |
| $r^2$ |  | 0.96 | 0.82 |  | 0.96 | 0.82 |  | 0.95 | 0.81 |  | 0.87 | 0.62 |

for all scenarios are reproduced by both ODC and Averaging techniques. The ODC technique has somewhat higher $T_B$ ranges than the True $T_B$ field, whereas the Averaging technique has lower ranges. The higher range for ODC technique is due to a very small number of high or low ODC $T_B$ values due to numerical instabilities near the boundaries of the study area. Overall, ODC technique represents the statistical distribution well as evidenced by the fact that the mean as well as the standard deviation of the ODC $T_B$ is similar to that of True $T_B$. On the other hand, the Average $T_B$ has lower standard deviation as well as a lower range compared to True $T_B$. The $r^2$ between True and ODC $T_B$ is also significantly higher than that between True and Average $T_B$. Over the entire study region, the statistics for ODC technique are much better than the Average technique (Table 4). In large part, the improvement can be attributed to the northern half of the study area, which is dominated by water bodies. High $T_B$ contrast between land and water allows the ODC technique to define the boundaries much better than the Averaging technique, leading to significantly lower errors in the vicinity of water bodies, particularly Lake Superior. Table 3 shows a similar analysis done for RMSE. It can be seen that the ODC technique produces even more pronounced improvements over Average technique. For each of the four scenarios, ODC technique generates about 50% of the RMSE as compared to the Averaging technique for the entire study area.

A significant portion of the earth's land mass is in proximity of water bodies, especially in the context of the rather large footprints produced by space-based microwave radiometers. Analysis of radiometer data has always been problematic for land areas adjacent to lakes and shorelines because of what is commonly referred as *contamination* from the water bodies. Results from the northern half of our study area demonstrate the efficacy of the ODC technique under such conditions. These results show that the ODC technique performs significantly better as measured by MAE and RMSE in the proximity of water bodies. It allows for a sharper delineation of the water bodies, while retrieving the data near the coastlines. The technique performs with accuracy similar to Averaging for region not dominated by water bodies as indicated by the southern half of the study area.

## 6. Conclusions

Optimal deconvolution of microwave brightness temperature observations provides better accuracy than a conventionally used averaging technique when producing spatially gridded images. The root mean square errors are reduced by about 50%

over the conventional technique under each of the four scenarios considered. The improvement is greatest in the vicinity of water bodies; in other areas the ODC technique performs similarly to or better than the conventional averaging technique.

The ODC technique can be effectively used in producing more accurate operational data products from a space-based radiometer, but it will require efficient management of the additional pre-processing computational burden placed by the technique. One possible solution is to create a priori "maps" of fractional contributions from the EASE grid cells in the observation field of view. For use with a conical scanning radiometer, these a priori maps will be a function of the earth–azimuth angle. To ensure higher accuracy, the maps can also be made a function of the placement of beam–center location within a region of the EASE grid cell in which it falls. Use of such methods to produce operational efficiencies and the computational efficiencies gained need to be explored further. Also, we have not assessed the possible sensor noise amplification as a result of ODC technique. These issues need to be addressed in detail before this technique can be used in operational environments.

Accurate estimation of $T_B$ is critical for several applications such as retrievals of soil moisture, sea ice extent as well as snow cover. In sea ice extent analysis, the ODC technique will be particularly helpful because of the large contrast between ice and water at microwave frequencies. With regards to soil moisture retrievals, the ODC technique may be significant in achieving the stated accuracy goal of ±4% soil moisture retrievals (Entekhabi et al., 2004) from upcoming space based missions (NASA's Hydrosphere State (Hydros) mission, and European Space Agency's Soil Moisture and Ocean Salinity (SMOS) mission). However, additional work needs to be done to quantify the improvements.

## References

Cavalieri, D. J., Gloersen, P., Parkinson, C. L., Comiso, J. C., & Zwally, H. J. (1997). Observed hemispheric asymmetry in global sea ice changes. *Science*, *278*(5340), 1104–1106.

Cosh, M. H., Jackson, T. J., Bindlish, R., & Prueger, J. (2004). Watershed scale temporal persistence of soil moisture and its role in validating satellite estimates. *Remote Sensing of Environment*, *92*, 427–435.

Crosson, W. L., Limaye, A. S., & Laymon, C. A. (2005). Parameter sensitivity of soil moisture retrievals from airborne L-band radiometer measurements in SMEX02. *IEEE Transactions on Geoscience and Remote Sensing*, *43*, 1517–1528.

Entekhabi, D., Njoku, E., Houser, P., Spencer, M., Doiron, T., Kim, Y., et al. (2004). The Hydrosphere State (Hydros) mission: An Earth system pathfinder for global mapping of soil moisture and land freeze/thaw. *IEEE Transactions on Geoscience and Remote Sensing*, *42*, 2184–2195.

Farrar, M. R., & Smith, E. A. (1992). Spatial resolution enhancement of terrestrial features using deconvolved SSM/I microwave brightness temperatures. *IEEE Transactions on Geoscience and Remote Sensing*, *30*, 349–355.

Laymon, C., Crosson, W., Jackson, T., Manu, A., & Tsegaye, T. (2001). Ground-based passive microwave remote sensing observations of soil moisture at S-band and L-band with insight into measurement accuracy. *IEEE Transactions on Geoscience and Remote Sensing*, *39*, 1844–1858.

Limaye, A. S., Crosson, W. L., Laymon, C. A., & Njoku, E. G. (2004). Landcover based optimal deconvolution of PALS L-band microwave brightness temperatures. *Remote Sensing of Environment*, *92*, 497–506.

Mo, T. (1999). AMSU-A antenna pattern corrections. *IEEE Transactions on Geoscience and Remote Sensing*, *37*, 103–112.

Njoku, E. (2004) updated daily. AMSR-E/Aqua L2B Surface Soil Moisture, Ancillary Parms, and QC EASE-Grids V001, Boulder, CO, USA: National Snow and Ice Data Center. Digital media.

Njoku, E. G., Jackson, T. L., Lakshmi, V., Chan, T., & Nghiem, S. V. (2003). Soil moisture retrieval from AMSR-E. *IEEE Transactions on Geoscience and Remote Sensing*, *41*(2), 215–229.

NSIDC (National Snow and Ice Data Center) (2002). EASE-grid: A versatile set of equal-area projections and grids. Available online at (http://nsidc.org/data/ease/ease_grid.html)

Poe, G. (1990). Optimum interpolation of imaging microwave radiometer data. *IEEE Transactions on Geoscience and Remote Sensing*, *28*, 800–810.

Robinson, W. D., Kummerow, C., & Olson, W. S. (1992). A technique for enhancing and matching the resolution of microwave measurements from the SSM/I. *IEEE Transactions on Geoscience and Remote Sensing*, *30*, 419–428.

Stogryn, A. (1978). Estimates of brightness temperatures from scanning radiometer data. *IEEE Transactions on Antennas and Propagation*, *AP-26: 5*, 720–726.

Vogelmann, J., Sohl, T., & Howard, S. (1998). Regional characterization of land cover using multiple sources of data. *Photogrammetric Engineering and Remote Sensing*, *64*(1), 45–57.

Wilson, W. J., Yueh, S. H., Dinardo, S. J., Chazanoff, S. L., Kitiyakara, A., Li, F. K., et al. (2001). Passive Active L-and S-Band (PALS) microwave sensor for ocean salinity and soil moisture measurements. *IEEE Transactions on Geoscience and Remote Sensing*, *39*, 1039–1048.